Silicon (2023) 15:7927–7941
https://doi.org/10.1007/s12633-023-02635-9

RESEARCH

Effect of Multipass FSP and ($SiC + TiB_2$) Nanoparticles on the Mechanical and Metallurgical Characteristic of the Hybrid Metal Matrix Composite

Bharat Singh Chittoriya[1] · Arvind Jayant[1] · Rakesh Kumar[1]

Received: 8 June 2023 / Accepted: 16 August 2023 / Published online: 24 August 2023

Abstract
In this work, a defect-free AA7050 ($TiB_2 + SiC$) hybrid surface composites was fabricated using multipass friction stir processing (MPFSP). The metallurgical characterization of the MPFSP/($SiC + TiB_2$)/AA7050 was analyzed by optical and scanning electron microscopes (SEM), and mechanical properties including tensile strength and microhardness were evaluated. All hybrid aluminum metal composite (AMC) had higher tensile strength and hardness values compared to the AA7050. Nanoparticles and FSP passes were able to break the coarse and elongated dendrite structure of the AA7050 and generated a homogenous and fine-grain structure in the stir zone (SZ). Among the different hybrid AMCs, the 4P FSP (25% TiB_2 + 75% SiC)/AA7050 composite exhibited the optimal dispersion of nanoparticles with a maximum tensile strength of 561 ± 7 MPa. The maximum hardness value of 4Pass FSP (25% TiB_2, 75% SiC)/AA7050 at the SZ was 179 HV, whereas the minimum microhardness value (161 HV) was perceived for 4P FSP (100% TiB_2)/AA7050. The maximum joint efficiency of 132.30% was perceived in 4P FSP (25% TiB_2, 75% SiC)/AA7050, while minimum joint efficiency of 111.39% was perceived in the 4P FSP (100% TiB_2)/AA7050.

Keywords Multipass FSP · Tensile properties · Microhardness · Microstructure · Nanoparticles

1 Introduction

Aluminum metal composite (AMC) is an advanced engineering material employed in various industries due to outstanding wear resistance and high specific strength [1–3]. It was observed that adding two or more nanoparticles to the aluminum metal composite could give advantages to each multi-phase reinforcement, resulting in outstanding mechanical characteristics [4]. Al_2O_3, SiC, and TiB_2 nanoparticles are extensively employed in the AMC due to their high tensile strength, wear resistance, hardness, and virtuous wettability [5–7]. All AMC vehicles of higher specific strength evolved by adding a hard particulate phase in softer aluminum alloys. The reinforcement particles are added via liquid phase processing, i.e., magnetic stir casting and stir casting, which contributes to the MMC's strength proportionally to its volume fraction. The hard nanoparticles/micro particles remain solid within the super-heated liquid matrix and expedite grain modification via nucleation. Many methods, including powder metallurgy [8], liquid metal infiltration [9], and stir casting [10], have been developed to manufacture AMCs—heterogeneous dissemination of the reinforcement particles during the above procedures and the resulting accumulation of nanoparticles. The importance of 7xxx series alloys has been identified in many industrial applications. It can be used in worm gears, meter shafts, missiles, aircraft, gears, sprockets, bike frames, etc. Because of the limitation of some properties of 7xxx alloys, researchers have attempted to enhance the mechanical and physical properties by incorporating one or more nanoparticles into metals via friction stir processing (FSP) [11, 12]. The strengthening phase identified as Guinier–Preston (GP) zones precipitate the alloy during the age-hardening process. The sequence of precipitates was determined as follows [13]. Supersaturated solid solution → GP zones → Intermediate precipitates ($MgZn_2$) → Equilibrium precipitates ($MgZn_2$). The strengthening pretentious by the precipitation aforementioned above

✉ Bharat Singh Chittoriya
bharat_pme2027@sliet.ac.in

[1] Department of Mechanical Engineering Sant Longowal Institute of Engineering & Technology, Longowal, Sangrur, India

is aging, and aging time and temperature are the two leading factors that manage the materialization of strengthening precipitates. The enhancement in the mechanical characterization depends on the precipitates' distribution, morphology, and size [14]. The precipitates coarsen and sometimes dissolve during thermos-mechanical processing at sufficient temperature and time, resulting in a noteworthy reduction in UTS [15] and microhardness value [16, 17] of this alloy. A significant improvement in the tensile properties may be attained by modifying its surface. These modifications can be done either by fabricating the surface composite or refining the microstructure by FSP with nanoparticles [18–21]. Numerous nanoparticles, including B_4C [22], TiB_2 [23], $SrCO_3$ [24], MWCNT [25], Ti_3AlC_2 [26], TiC [27], MoS_2 [28], SiC [29], were used to fabricate MMC using FSP to enhance the metallurgical characterization of the composite alloys. The excellent dispersion of the nanoparticles and grain modification in the AMC leading in low thermal expansion, high corrosion and wear resistance. The effect of FSP parameters on wear resistance, hardness, and microstructure of AA7075/SiC was examined and revealed that the traverse speed (TS) affected the composite quality. FSP pass and TRS pretentious the dissemination of nanoparticles through the matrix. The hardness of base metal was improved twice, enhancing the wear properties [30]. Two reinforcement particles, Al_2O_3 and TiB_2, were employed on AA7050 through single-pass FSP. The nanoparticles were observed to be homogeneously disseminated over the SZ. The accumulation of nanoparticles was not perceived in the FSPed specimens resulting in higher strength than the base metal [31]. By adding micro-sized particles, TiB_2 in AA7050 exhibited higher elastic modulus, and smaller grain size enhanced the mechanical properties over the unreinforced AA7050. TiB_2 enhances the fatigue characteristics in the MMC because TiB_2 micro particles impended dislocations from piling up at the inclusion and delaying the crack initiation [32]. Hybrid surface composite (HSC) with two different nanoparticles (MoS_2 and B_4C)/AA6061 via FSP was successfully fabricated and enhanced the tribological and mechanical properties of the base metals. The wear resistance and hardness value of the composites were improved due to uniformly distribution of the nanoparticles, grain refinement and dispersion hardening [33, 34]. HSC with more than two nanoparticles have gained attention due to their superior mechanical and tribological properties, however, conventional liquid-phase processing methods can lead to the materialization of undesirable brittle intermetallic compound. The FSP give promising solution to overcome these issue effectively [35]. The effect of tool pin profile on the temperature distribution in Al-Si/FSP was examined, and it was observed that when the TS increases, both the longitudinal and tool axial forces increase and decrease as the TRS increases [36]. Based on the Eulerian–Lagrangian, the finite element method was developed and investigated the temperature distribution, material flow, and metallurgical characterization of Al-Si alloys and then verified by the experimental results and perceived that the simulation model revealed good agreement with experimental results [37]. TiC nanoparticles were employed to improve the wear and tensile properties of Al-Si alloys. It was perceived that excellent bonding between Al-Si alloy and TiC nanoparticles and particle distribution occurs in the SZ [38]. The response surface methodology optimization technique was employed to envisage the responses of the FSP of A356/B4C, and it was observed that the model was adequate at a 95% confidence interval. The author suggested that the TS was the prevailing factor in improving the strength of the processed region [39]. The plastic deformation and frictional heat are the primary mechanisms for increasing the temperature of the parent material, while the rotating tool pin cannot alone generate the strain and heat within the samples, and approximately 92% of the heat is generated by the tool shoulder [40]. FSP with nanoparticles ($TiB_2 + SiC$) contributes to innovation by revolutionizing the fabrication of advanced engineering materials. The incorporation of TiB_2 and SiC nanoparticles during FSP results in significant improvements in mechanical properties, including enhanced strength, toughness, and wear resistance. This innovation enables the improvement of tailor-made materials with superior performance characteristics, offering new possibilities for various industrial applications in sectors such as transportation, aerospace, and manufacturing. The enhanced properties of these nanocomposites open doors to innovative solutions, pushing the boundaries of material science and engineering and driving progress in diverse fields.

The nanoparticle selection depends on the nanoparticles' compatibility with the metal matrix. Authoritatively SiC and TiB_2 offer excellent mechanical and thermal properties. This work aims to use two different reinforcement particles (TiB_2 and SiC) to enhance the base metal's metallurgical characteristics by MPFSP technique and homogeneously disseminated nanoparticles over the processed zone. To the author's best knowledge, this combination has not been examined.

2 Materials and Methods

The base plate AA7050 with a dimension of $180 \times 70 \times 4$ mm was used, and SiC and TiB_2 nanoparticles with a mean particle size of 15 ± 7 nm were used as reinforcements. U groove was made at the center of the parent material via a shaper machine, and the reinforcement particles (SiC and TiB_2) were added with dimensions of $170 \times 2.5 \times 2.5$ mm. The groove was closed via a pin less tool with a TRS of 1200 rpm, and TS of 100 mm/min, where the FSP tool stirred the nanoparticles with the base material. The

combination of TiB_2 and SiC nanoparticles was used due to its ability to improve the properties of the processed material. When combined, these reinforcement particles work synergistically to further improve the mechanical characteristics of the material, making it stronger and more durable. The presence of TiB_2 and SiC nanoparticles during FSP promotes grain refinement in the microstructure of the welded material. The nanoparticles act as effective nucleation sites for recrystallization, leading to the materialization of finer and more uniform grains. This grain refinement contributes to increased strength and toughness, ensuring the material can withstand mechanical stresses and harsh conditions. They can also withstand the elevated temperatures generated during the FSP process, ensuring that they remain dispersed and maintain their reinforcing effects in the final material. The synergistic effects arising from the combination of TiB_2 and SiC nanoparticles further amplify the overall properties of the processed material. Together, they offer improved performance beyond what each nanoparticle can achieve individually, making the resulting material highly desirable for various engineering applications. The square pin profile was used during the FSP process made of tempered H13 tool steel because it gives better heat transfer and material mixing during the MPFSP, leading in a uniform grain structure and enhanced tensile properties and hardness value [41, 42]. The square pin's design induces a higher number of pulsating actions, leading to intense frictional heating at the welding interface. This heat generation is crucial for achieving the necessary plasticization and mixing of the materials without reaching their melting points. Additionally, the square pin profile promotes effective mixing of the materials being processed [43]. The distinct shape of the square pin facilitates vigorous stirring and material flow, resulting in a more uniform dissemination of alloying elements, nanoparticles, or other additives within the weld region. This uniform mixing leads to enhanced properties and performance of the welded joint. Moreover, the intensive stirring action caused by the square pin contributes to grain refinement. The material experiences grain size reduction, leading to a finer microstructure, which, in turn, improves mechanical properties. The efficient mixing and stirring action help reduce the occurrence of voids, porosity, and inclusions, ensuring better weld integrity and overall quality of the final product. The dimension of FSP tool and tensile test specimen was demonstrated in Fig. 1. A fixture was used to hold the base plate during the FSP process and prevent it from being misaligned or moving. Misalignment can lead to poor joint quality, defects, or even failure of the joints. The tilt angle, axial force, TS, and TRS were kept constant at 2°, 7.2 kN, TRS-1200 rpm, and TS-100 mm/min respectively. Only nanoparticles were varied during the experimentation. The input parameters of MPFSP was demonstrated in Table 1.

A groove, 170 mm long, 2.5 mm deep, and 2.5 mm wide, was machined at the specimen's center to facilitate nanoparticle (SiC and TiB_2) dispersion. The volume fraction (VF) of these nanoparticles within the groove was determined using specified equations [44].

$$\mathrm{VF}(\%) = \frac{\mathrm{GroovedArea}}{\mathrm{Projectedareaoftool Pin}}$$

$$\mathrm{Groovearea} = \mathrm{Groovedepth} \times \mathrm{Groovewidth}$$

The reinforcement particles ($TiB_2 + SiC$) were varied and incorporated with AA7050 matrix to achieve 0, 25, 50, 75, and 100 vol. % of both nanoparticles. The grooves were strongly packed with both reinforcement particles. Primarily, the groove top surface was covered by processing with a pin less tool to hinder the expulsion of SiC and TiB_2 reinforcement particles.

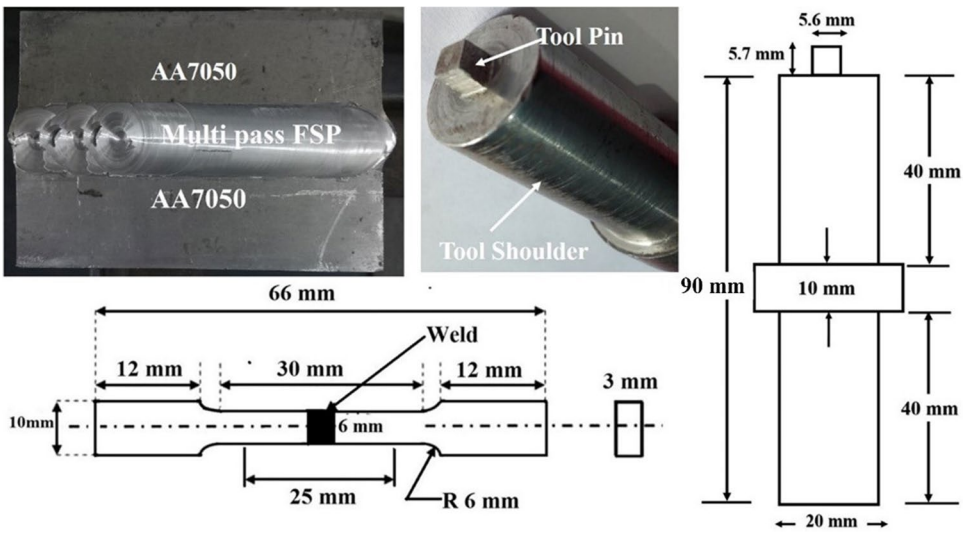

Fig. 1 Experimental process of MPFSP

Table 1 Process parameters of MPFSP of AA7050

S.No	Sample Designation	TRS (rpm)	TS (mm/min)	FSP pass	TiB_2 volume %	SiC volume %
1	AA7050	TRS-1200 rpm	TS-100 mm/min	4	0	0
2	100% SiC				0	100
3	100% TiB_2				100	0
4	75% TiB_2, 25% SiC				75	25
5	25% TiB_2, 75% SiC				25	75
6	50% TiB_2, 50% SiC				50	50

The specimens for tensile testing were sliced under the ASTM E8 standard precisely along the processed area. Before undergoing the tensile test, these specimens were meticulously polished using emery papers within the 400 to 800 grade range. Employing a constant strain rate of 2×10^{-1} s^{-1} at room temperature, the tensile tests were carried out on a UTM machine (Olsen Tinius: H50KS: 50 kN). Both optical and SEM methods were employed, to assess the microstructure within the processed region. The SEM specimens underwent a polishing procedure using emery papers graded between 600 and 2200. Subsequently, these specimens were subjected to etching with Keller's reagent, which comprises a mixture of 82 ml of H_2O, 4 ml of HF, 6 ml of HCl, and 8 ml of HNO_3. The SEM machine utilized for this examination possessed a resolution of 2.0 nm @3 kV. For assessing hardness, the Vickers hardness test was performed in line with the ASTM E384 standard. A Vickers hardness machine was utilized with a 120 g load applied for 10 s at room temperature. The preparation of Transmission Electron Microscopy (TEM) specimens involved electro polishing. The specimens were immersed in a solution consisting of 70% CH_3OH and 30% HNO_3, operating at a temperature of -20 °C and an applied voltage of 10 V. This procedure facilitated the analysis of dislocation precipitates, grain boundaries, and dislocation walls. These parameters are commonly used in micro-indentation testing and are chosen to ensure consistent and repeatable results.

3 Results and Discussion

3.1 Microstructural Observation

The microstructure of the AA7050/(SiC + TiB_2) hybrid metal matrix processed zone was analyzed, and observed the onion rings in the SZ and it was expected that the numerous onion rings' production would correspond to the sharp edges of the FSW tool. The flow pattern of complex material with multiple onion rings in the SZ was depicted in Fig. 2. The generation of the mixed sub-layers could be explained by the fact that the plasticized materials in the vicinity of the regions may have met high turbulence and had sufficient time to be thoroughly mixed before finally being deposited into the wake of the FSPed/(SiC + TiB_2) joints. AA7050 has achieved partial penetration. In the mixed flow zone, there are alternate lamellae for base alloys. A multifaceted flow pattern was visible in the MPFSP zone.

The flow of plasticized material was illustrated to be significantly superplastic in the mixed flow region, which causes an erratic intercalation pattern. The plasticized material was moved layer by layer to create a lamellae structure. Reinforcement particles (SiC + TiB_2) are vigorously mixed and penetrated in the base metal. The input heat and material flow are affected by the FSP parameters [45]. The process parameters combinations produced good-quality welds. The excellent joints were also fabricated using various nanoparticles. The addition of TiB_2 and SiC in the processed region improved the welding conditions, i.e. material deformation

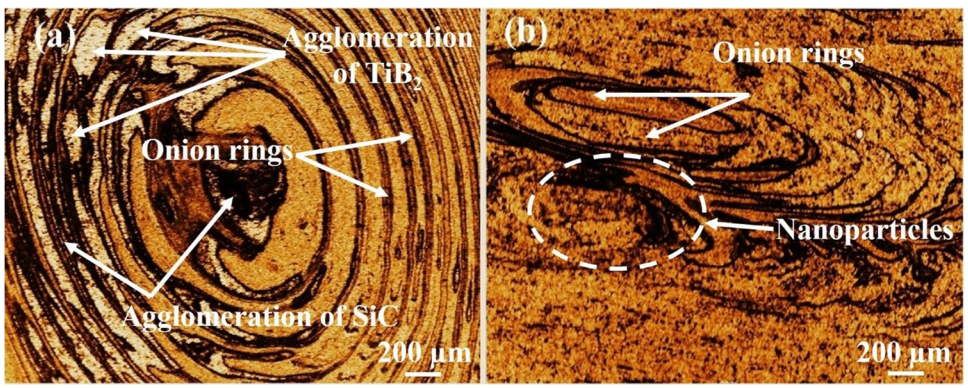

Fig. 2 Formation of onion rings and Zigzag lines, (**a**) specimens No-1, (**b**) Specimens No-5

and heat generated. Increasing the TRS at a given TS and decreasing the TS at a constant TRS causes the input heat in the welded region to increase [46].

In contrast, considering the alteration of TRS and TS, the material plasticized flow due to stirring action is changed. The multipass positively affected the weld characteristics of the processed region. Due to generated heat and strange stirring, the discontinuity between the TMAZ and SZ was developed [47]. There is no accumulation of defects between the TMAZ and SZ.

The optical images of the FSPed zone of the AA7050/($SiC + TiB_2$) were revealed in Fig. 3, and it was observed that the dissemination of SiC and TiB_2, welding parameters, heat input, and intermetallic compound have a conspicuous role in the metallurgical characterization of the processed zone. The worst mechanical properties were perceived at the high TRS and low TS [48]. The grain size of the AA7050 reveals 142 µm. The TMAZ and HAZ preserve severe inhomogeneity chemical and physical properties, showing discontinuous banded structure resulting in coarse grains. The grain distribution in the HAZ was inhomogeneous, and the structures were coarsening and elongated. The most strengthening phases in the HAZ may be reduced by re-dissolution during FSP due to rapid cooling and high temperature. The TMAZ and HAZ perceived a sharp interface on AS and uncertainty on the RS, which reveals that the AS has some more significant gradients of strain and temperature [49, 50]. The interface slope between the SZ and TMAZ was more influential on the RS, which can be attributed to the disseminated reinforcement particles and the material flow [51]. TMAZ experienced partially recrystallized and weaker deformation than the SZ, resulting in equiaxed DRX and elongated deformation perceived on the TMAZ side. The robust and diverse structure was generated due to eutectic precipitates Mg_2Si, which dissolved utterly in the AMC during FSP [52]. A high agglomeration of TiB_2 and SiC was observed in a 1-pass FSP (Fig. 3a). The homogeneousness of the TiB_2 and SiC reinforcement particles modified as the FSP passes increased because severe plastic deformation followed by the SiC and TiB_2 agglomeration breaking and material flow occurred demonstrated in Fig. 3d. The high magnification OM images of MPFSP (25% TiB_2, 75% SiC)/AA7050 at the stir zone revealed in Fig. 4. 1P FSP observed that material mixing and thermoplastic deformation of the base metal in the square pin should be insufficient and inhomogeneous. The banded particles' poor regions gradually decrease as the FSP's passes increase. After 4-passes of FSP, the nanoparticles were uniformly dispersed throughout the material without any agglomeration resulting in a uniform structure revealed in Fig. 4d. This uniformity was achieved through accumulative plastic deformation, which was the process of repeatedly applying pressure to a material to reshape and deform it.

To analyzed the influence of ($TiB_2 + SiC$) nanoparticles and multipss FSP of AA7050, the grain structure and dispersion of nanoparticles in the SZ was analyzed. Figure 5 reveals the SEM images of MPFSP (25% TiB_2, 75% SiC)/AA7050 at the SZ. The defect-free zone of AA7050 with

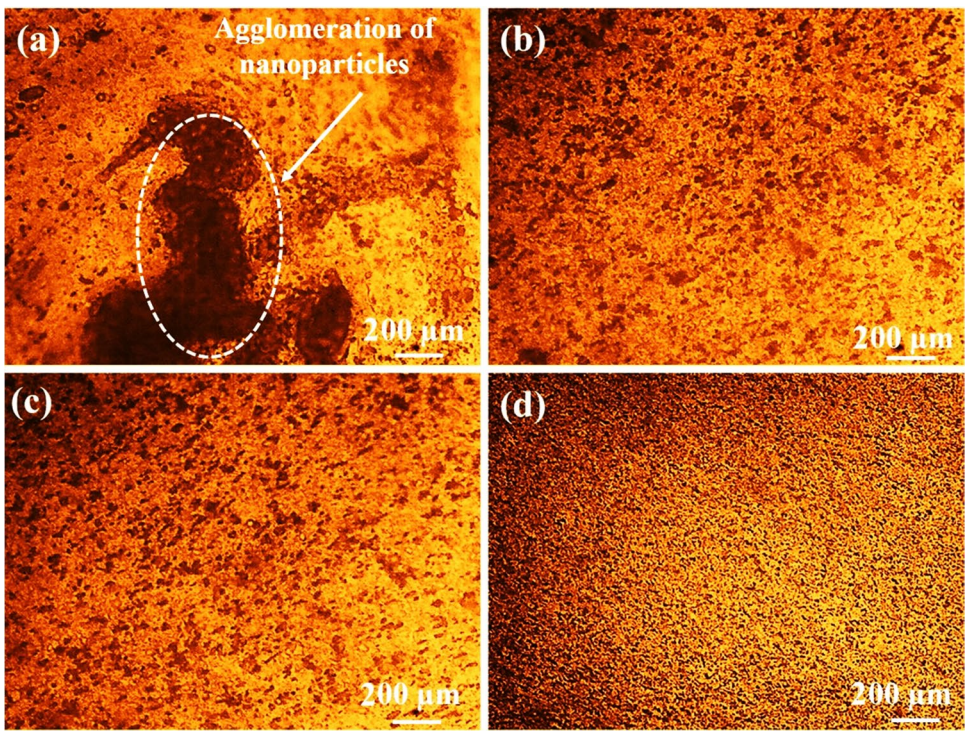

Fig. 3 Friction stir processing of AA7050/($SiC + TiB_2$), (**a**) 1st pass, (**b**) 2nd pass, (**c**) 3rd pass, (**d**) 4th pass

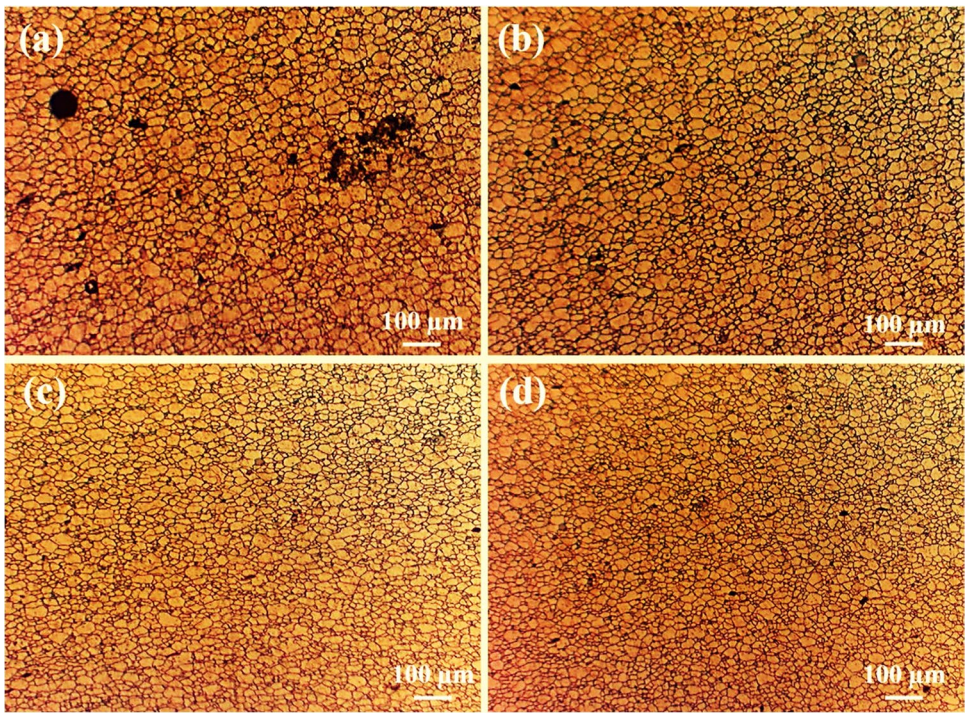

Fig. 4 OM images of multi pass FSP (25% TiB_2, 75% SiC)/AA7050, (**a**) 1st pass, (**b**) 2nd pass, (**c**) 3rd pass, (**d**) 4th pass

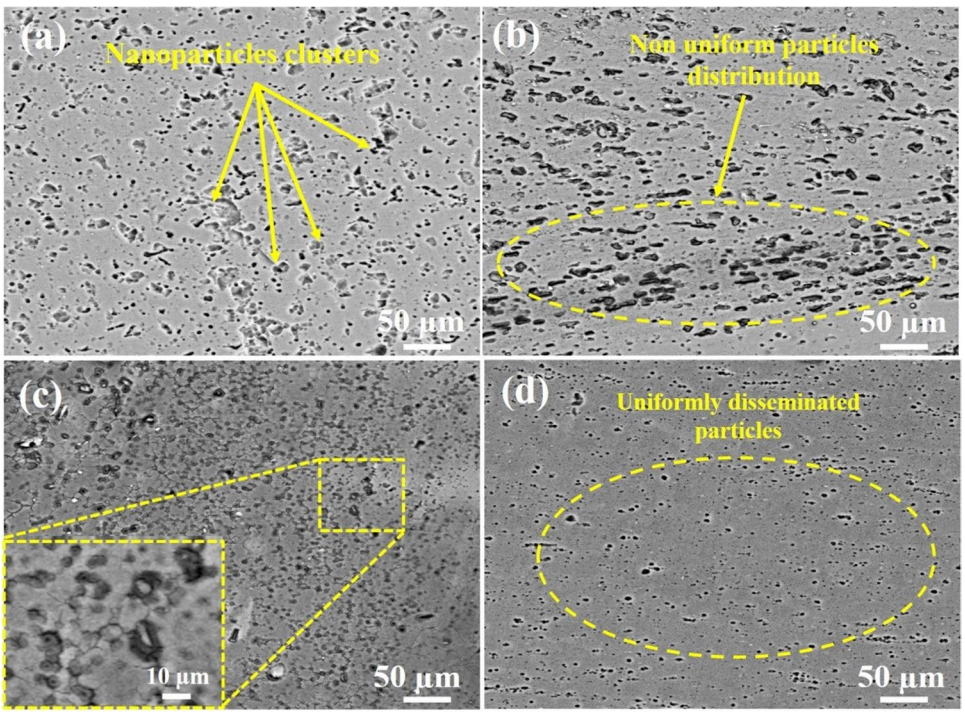

Fig. 5 FESEM image of multi pass FSP (25% TiB_2, 75% SiC)/AA7050, (**a**) 1st pass, (**b**) 2nd pass, (**c**) 3rd pass, (**d**) 4th pass

the appropriate intermixing of reinforcement particles was perceived in the 4 Pass FSP, as represented in Fig. 5d. The microstructure of SZ was characterized by reinforcement particles SiC, TiB_2 and primary α-Al where α particles were observed along the grains boundary. The HAZ perceived a low heat generation than the SZ, resulting few α-particles precipitated out at grain boundaries and fewer α-Al particles in the HAZ. The modification of the α-Al exist in the base metals was uninterruptedly enhanced as the as the reinforced particles added. Due to improvement of dispersion and material mixing, the Mg_2Si precipitates were further decimated. The clustering of nanoparticles and worst bonding between the AA7050 and (SiC + TiB_2) was observed at the SZ in single pass FSP, revealed in

Fig. 5a, which implies that a single FSP pass was not sufficient to prevent the clustering of the nanopaticles due to insufficient strain developed by the tool's stiring action [53]. However, when the FSP passes increased from one to four, the clustring of the ($SiC + TiB_2$) nanoparticles became less prominent and the dispersion pattern became more uniform. In the two-pass FSPed region, shown in Fig. 5b, a non-uniform dispersion pattern of ($SiC + TiB_2$) reinforcement particles was observed [54, 55]. However, the dispersion pattern improved after three passes of FSP. The homogeneousness of the reinforcement particles in the SZ of the four-pass FSP sample was confirmed by EDS mapping demosntrated in Fig. 6. The rejection or engulfment of nanoparticles can directly affect the growth mechanisms of the aluminum matrix composites. The dendrites may grow freely on the advancing side, generating large dendrites. Increasing the SiC and TiB_2 reinforcement particles restricted the growth of dendrites. The high hardness value and large 2nd dendrite arm spacing reveal are indicative of Orowan-type strengthening being the dominant mechanism [56, 57]. Orowan-type strengthening refers to the strengthening of a material due to the presence of a high density of obstacles to dislocation motion, such as precipitates or 2nd phase particles. The dendrite size in 4 pass FSP (25% TiB_2, 75% SiC)/AA7050 was intense smaller than the other AMCs. Increasing the reinforcement particles can lead to the formation of large agglomeration particles, which can overcome repulsion forces during solidification and be captured inside grains. This process may result in the formation of large dendrites, which are a characteristic of solidification processes. The presence of these large dendrites, combined with the high hardness value, suggests that the material has undergone strengthening through both Orowan and Hall–Petch mechanisms. The large dendrites may act as obstacles to dislocation motion and contribute to Orowan strengthening, while the small grain size resulting from the solidification process may contribute to Hall–Petch strengthening.

The clusters tend to be preserved when the reinforced particles are mixed with the base metal. The nanoparticles were in the interstices between the AA7050 grains, and the pressing was deformed. Compaction and simple mixing did not break up the micro-clusters. Figure 5a-d reveals the synthesized nanocomposites' SEM images for different reinforcement volume fractions. The agglomeration of nanoparticles SiC and TiB_2 increases by increasing the nanoparticle's volume fraction. Generally, fewer voids and porosity results to a greater density of the samples [58]. Moreover, the high magnification SEM images indicate SiC and TiB_2 reinforcement particles disseminated among the Al matrix. The Van der Waals force is a weak attractive force that arises between atoms or molecules due to temporary or induced dipoles in the electron distribution. It is one of several interatomic forces that contribute to the adhesion or cohesion of solids. In the case of TiB_2 and SiC reinforcement particles, the Van der Waals force between TiB_2 particles is stronger than that between SiC particles, which can lead to more agglomeration of TiB_2 particles. This can in turn lead to a higher number of pores in Al-TiB_2 samples compared to Al-SiC samples.

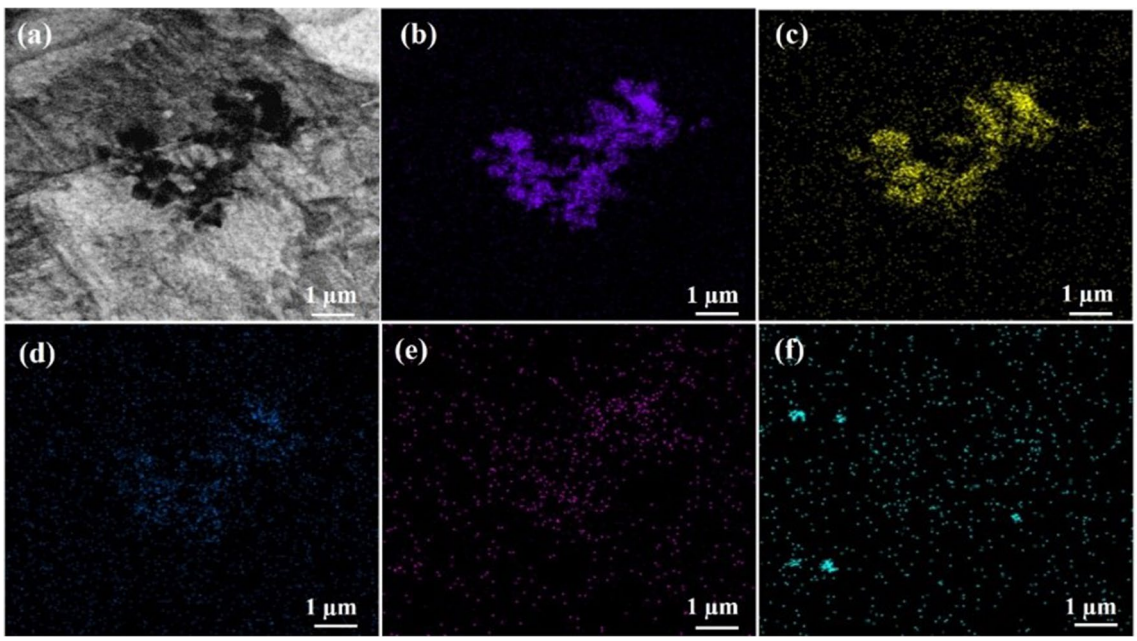

Fig. 6 Mapping of 4P FSP of AA7050/($SiC + TiB_2$)

Overall, in MPFSP, each pass contributes to severe plastic deformation and generates localized heat, causing DRX and grain refinement. As the process is repeated four times, the cumulative effect leads to a significant reduction in grain size, resulting in a finer and more homogenous microstructure compared to the as-received material. The multiple passes also serve to homogenize the microstructure by breaking down coarse-grained regions and promoting recrystallization throughout the material. The addition of ($SiC + TiB_2$) nanoparticles further enhances the microstructural properties of AA7050 alloy. The nanoparticles, known for their high hardness and strength, are dispersed uniformly within the aluminum matrix. During the FSP process, these nanoparticles act as efficient nucleation sites, facilitating the formation of fine and well-distributed grains upon recrystallization. This uniform grain structure contributes to improved mechanical properties. The nanoparticles also play a crucial role in particle pinning and grain boundary strengthening. Their small size and high volume fraction impede grain boundary movement and inhibit grain growth during processing and subsequent heat treatments. As a result, the microstructure remains stable, preventing the coarsening of grains and enhancing the mechanical properties over prolonged service life. The successful incorporation of ($SiC + TiB_2$) nanoparticles into the AA7050 alloy depends on achieving a uniform distribution of nanoparticles throughout the matrix..

Due to discontinuities, material flow, and cracks around the agglomerated SiC and TiB_2 nanoparticles in the SZ was perceived in single-pass FSP, these flaws were removed by the multipass process demonstrated in Fig. 7a, b. The TiB_2 and SiC reinforcement particles and AA7050 were compressed by the rotating FSP tool during the plunging stage. When the tool bottom and reinforcement particles come into contact, the reinforcement particles transfer to the side faces, forming a processed region [59]. After the 4th pass FSP, no gap was found between the AA7050 and reinforcement particles due to homogenous particle dispersion. The fine secondary phases were generated in the processed region, this may be related to deformation fragmentation and dissemination of nanoparticles that occurred at the SZ. Evidence of low dislocation density and precipitated phases was perceived in the composite region due to the dissolved strengthening phases in the processed zones, which gives a direct correlation between precipitation growth, dissolution, and fracture load [60]. A small number of precipitates were wound off by the dislocation, which also expanded the interface area and increased the interface energy [61, 62]. The resulting fine-grained, and new phases seem like solid-state reactions. The recrystallized grains appear to have an absence of precipitates and dislocations within the grain boundary. This suggests that the recrystallization process where new grains with fewer defects were formed. The deep penetration exhibited apparent cracks, indicating that the single-pass FSP was delicate and did not achieve proper penetration. The elongated and coarse grains observed in the SZ show uniform dislocation dissemination. These grains are pinned by the hardening precipitates, which contribute to their strength and mechanical properties.

3.2 XRD Analysis

XRD pattern was generated to examine the phase detection with Cukα radiation at 1.518 Å of MPFSP/($SiC + TiB_2$) as shown in Fig. 8. Transforming the diffraction peaks to d spacing allows for alloy identification. The TiB_2, SiC, and Mg_2Si peak shows the incongruently noticeable confirmation of AMC joints. The other peaks, except TiB_2, SiC, and Mg_2Si, Si, and Al, were not observed in the XRD graph, which shows the thermal steadiness of existing peaks. The TiB_2 and SiC intensity was reduced as the FSP pass increased from one to four. $\tau = Sin\theta$. $cos\psi 2\ \mu$ analyzed the depth of penetration of the weldment [63], where τ is the penetration depth, ψ is the tilt angle, μ is the coefficient of linear absorption, and θ is the Bragg peak. The MPFSP helped to reduce the agglomeration of reinforcement particles in modified surface of AA7050/($TiB_2 + SiC$), resulting in a finer and uniform grain structures. The modified particles helped to alleviate the load of Marangoni convection effect, which improved the fluidity of the base metal

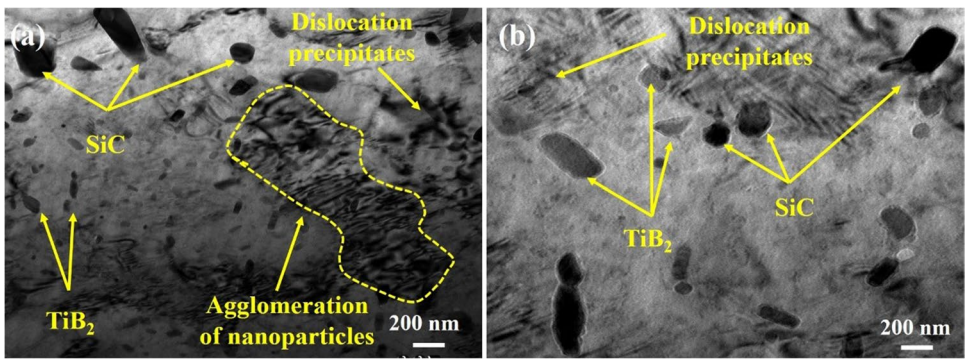

Fig. 7 TEM analysis of multipass FSP/($SiC + TiB_2$), (**a**) Single pass FSP, (**b**) Four pass FSP

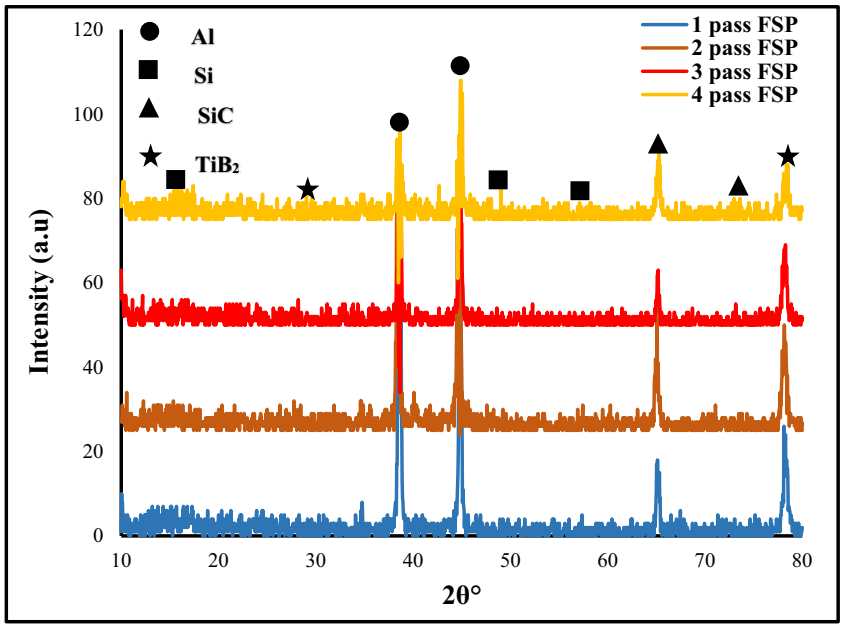

Fig. 8 XRD analysis of MPFSP/(SiC + TiB_2) of AA7050

resulting in more even distribution of the nanoparticles. The microhardness value of the weldment was affected by the boundary energy, strain hardening, and precipitate generation [64]. The coarse precipitates SiC and TiB_2 were converted into small phases when the FSP pass increased. During analysis, there was no unfavorable reaction found between the welded zone. The influence of grains size on the solid-solution, precipitate, and dislocation density was immaterial [65, 66]. Precipitation growth involves the nucleation, coarsening, and dissolution of the precipitate.

The effect of MPFSP and the SiC + TiB2 nanoparticles on the X-ray diffraction (XRD) peaks of AA7050 alloy is a reduction in peak intensity and broadening of diffraction peaks. This leads to a decrease in the size of coherent scattering domains and causes peak broadening in the XRD pattern. Additionally, the presence of (SiC + TiB2) nanoparticles creates lattice distortions and dislocation densities around the nanoparticles, contributing to peak broadening as well. The uniform distribution of nanoparticles and the fine-grained microstructure resulting from the combination of 4-pass FSP and nanoparticle incorporation contribute to the observed changes in XRD peaks, indicating improvements in the crystalline structure and enhanced mechanical properties of the AA7050 alloy.

3.3 Tensile Strength

The UTS of MPFSP/(SiC + TiB_2)/AA7050 were investigated by the UTM machine. The joint efficiency, % strain, and microhardness of the multipass AMCs were observed to improve as the FSP passes increased. This improvement was attributed to the modification of the SiC and TiB_2 nanoparticles, which led to improved tensile strength. The true stress strain curve of the AMC revealed that the both nanoparticles significantly affected the tensile strength. The UTS of the MPFSP/(SiC + TiB_2)/ AA7050 increased from 424 ± 5 to 561 ± 7 MPa as the number of FSP passes increased, which can be attributed to the fine grain structure and high fraction of high-angle grain boundaries obtained by MPFSP. Grain refinement can enhance the tensile properties of materials, including the UTS and % strain. The homogenous dissemination of the 2^{nd} phase particles (SiC and TiB_2) within the aluminum matrix also contributed to the improvement in the UTS. This is because the 2^{nd} phase particles can act as obstacles to dislocation motion, which can strengthen the material. Additionally, the grain refinement resulting from the FSP process can increase the compatibility of neighboring grains, which can enhance the percentage strain. In the 2^{nd} phase, uniform crystal dissemination is the leading barrier to dislocation motion, enhancing the tensile strength of AMCs. Due to the dissolution of coarse TiB_2, SiC and Mg_2Si, and grain refinement, a maximum tensile strength (561 ± 7 MPa) was perceived in 4P FSP (25% TiB_2, 75% SiC)/AA7050, which significantly increases the ductility and decreases the crack's growth rate, demonstrated in Table 2. With high stress concentration and sharp grain size, poor tensile strength was found in the TMAZ. The fracture at the HAZ occurred due to distortion, irregular grain structure, and heat effect. The dissolution and defects of the precipitates were formed by insufficient heat input, which has a deleterious influence on the joint's performance. The maximum joint

Table 2 Mechanical properties of the MPFSP/(SiC + TiB_2) of AA7050

S.No	Sample Name	TRS (rpm)	TS (mm/min)	FSP pass	UTS (MPa)	% elongation	Joint efficiency (%)	Hardness at SZ (HV)
1	AA7050	-	-	-	424 ± 5	10.52	-	132
2	100% SiC	1200	100	4	489 ± 3	11.89	115.46	169
3	100% TiB_2				472 ± 4	12.14	111.39	161
4	75% TiB_2, 25% SiC				513 ± 5	12.74	120.99	174
5	25% TiB_2, 75% SiC				561 ± 7	13.23	132.30	179
6	50% TiB_2, 50% SiC				524 ± 4	13.14	123.60	166

efficiency of 132.30% was perceived in 4P FSP (25% TiB_2, 75% SiC)/AA7050, while minimum joint efficiency of 111.39% was perceived in the 4P FSP (100% TiB_2)/AA7050. Additionally, metal matrix composite specimens with two nanoparticles fratured outside the SZ suggests good bonding between the nanoparticles and the base metal, and good nanoparticles dissemination in the metal matrix composite. The combination of MPFSP and the addition of (SiC + TiB2) nanoparticles to AA7050 alloy leads to significant improvements in tensile strength from 424 ± 5 MPa to 561 ± 7 MPa. The MPFSP refines the grain structure, and the uniform dispersion of nanoparticles within the aluminum matrix impedes dislocation movement and acts as effective strengthening. This results in enhanced solid solution strengthening, work hardening, and particle pinning effects, leading to increased resistance to plastic deformation and improved tensile strength of the AA7050 alloy, making it more suitable for high-strength applications in aerospace and structural engineering.

3.4 Microhardness Analysis

The microhardness profile of MPFSP (TiB_2 + SiC)/AA7050 was demonstrated in Fig. 9. The hardness variation was observed due to the inhomogeneous of the grain structure. The microstructure is the controlling factor for enhancing microhardness. The temperature variation, particle density, and strain rate also affect the microhardness value [67], resulting in strain hardening. A low strain rate and smaller grain size convinced strain hardening of the MPFSP (TiB_2 + SiC)/AA7050. Due to inadequate material flow engendered by the rotating tool, inhomogeneity of hardness value in the stir zone occurred [68]. The MPFSP (TiB_2 + SiC)/AA7050 perceived refined grains structure to have a higher microhardness value per the Hall–Petch relationship. The microhardness value was higher if the indenter was positioned neighboring the Mg_2Si rather than the α-Al. The hardness indentation of MPFSP was shown in Fig. 10. Conversely, the microhardness value was perceived to be low. The maximum hardness value of 4pass

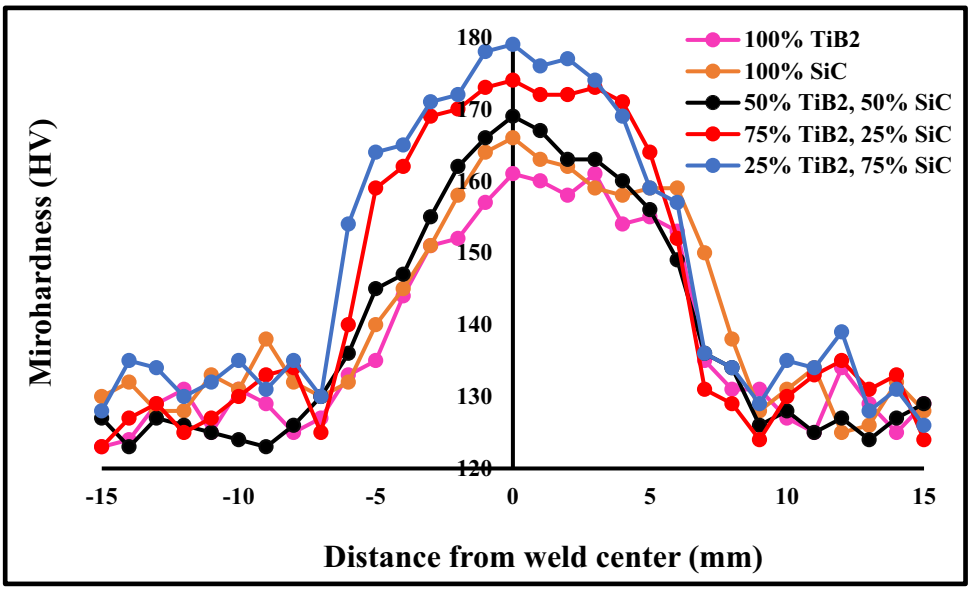

Fig. 9 Hardness distribution profile of mutipass FSP (TiB_2 + SiC)/AA7050

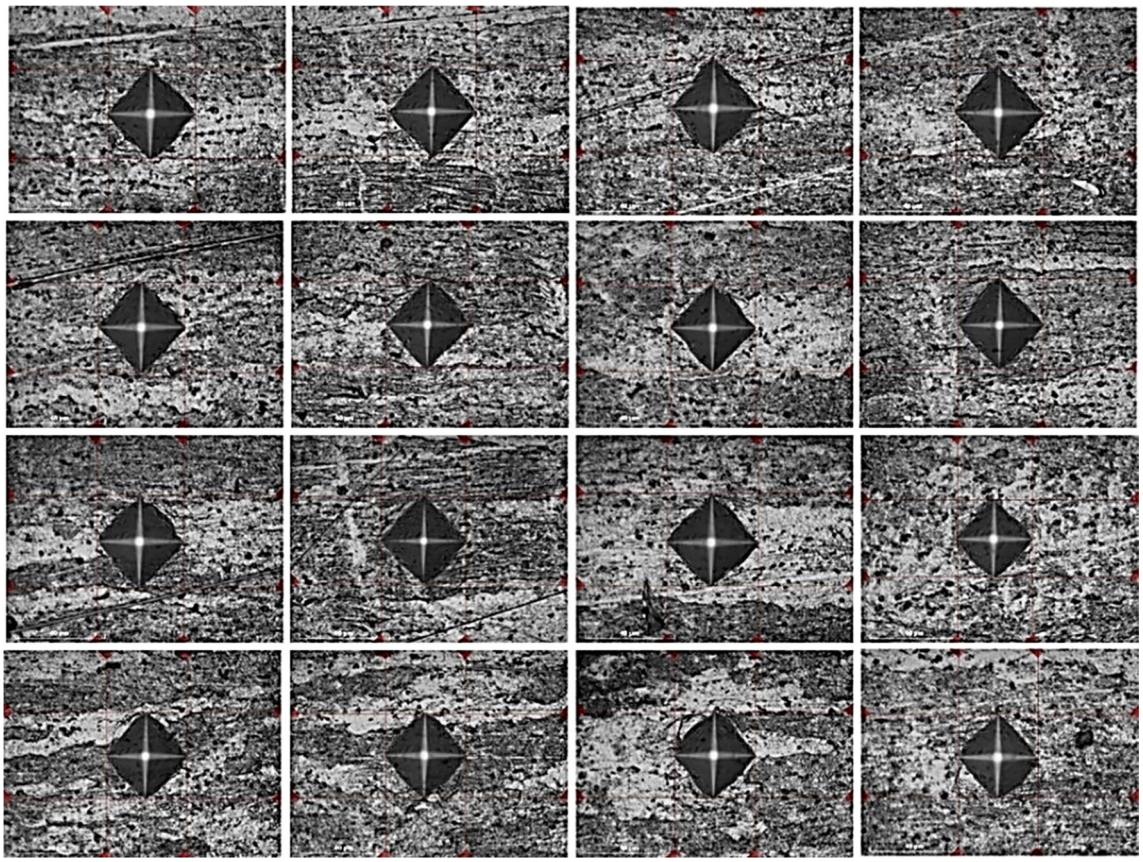

Fig. 10 Hardness indentation of MPFSP (TiB_2 + SiC)/AA7050

FSP (25% TiB_2, 75% SiC)/AA7050 at the SZ was 179 HV, while the minimum microhardness value (161 HV) was perceived for 4P FSP (100% TiB_2)/AA7050. With the steady fall in the microhardness in the HAZ, the partially dissolved and strengthening phase coarsen in the HAZ, and some precipitates dissolve in the TMAZ region [69]. The addition of nanoparticles SiC and TiB_2, can further improved the processed AMC properties. The microhardness profile of a MPFSP with SiC and TiB_2 nanoparticles can be affected by several factors, such as the processing parameters, the size and dissemination of the reinforcement particles, and the microstructure of the base material. Usually, the addition of nanoparticles to a material can increase its microhardness due to the occurrence of nanoparticles in the microstructure. During FSP, the nanoparticles are dispersed into the material and can be further refined by the stirring action. The repeated passes of the FSP tool over the material can lead to a homogenized distribution of the nanoparticles, resulting in a more uniform microhardness profile. Higher TS and TRS can result in higher strain rates and more severe deformation, leading to a finer microstructure and higher microhardness. Conversely, lower rotational speeds and traverse speeds can result in coarser microstructures and lower microhardness. In addition, the size and dissemination of the reinforcement particles can also affect the microhardness profile of the processed material. Nanoparticles with smaller sizes and more uniform distributions can lead to a more uniform dispersion of strengthening particles, resulting in a more uniform microhardness profile. The microhardness value variation of MPFSP (TiB_2 + SiC)/AA7050 was observed in the range of 160–180 HV due to improvement of grain refinement and dislocation density in the SZ.

3.5 Fractography

The SEM fractography of MPFSP (TiB_2 + SiC)/AA7050 surface composite was revealed in Fig. 11. The surface composite was fabricated with varying volume percentages of nanoparticles (TiB_2 and SiC). The presence of dimples on the matrix indicates that the material underwent plastic deformation before fracturing, which is characteristic of ductile fracture [70]. The fact that nanoparticles were pulled away from the matrix suggests that there was good bonding between the matrix and nanoparticles, which is desirable in a composite material. However, the increased dislocation density on the surface of the composite can lead to a reduction in

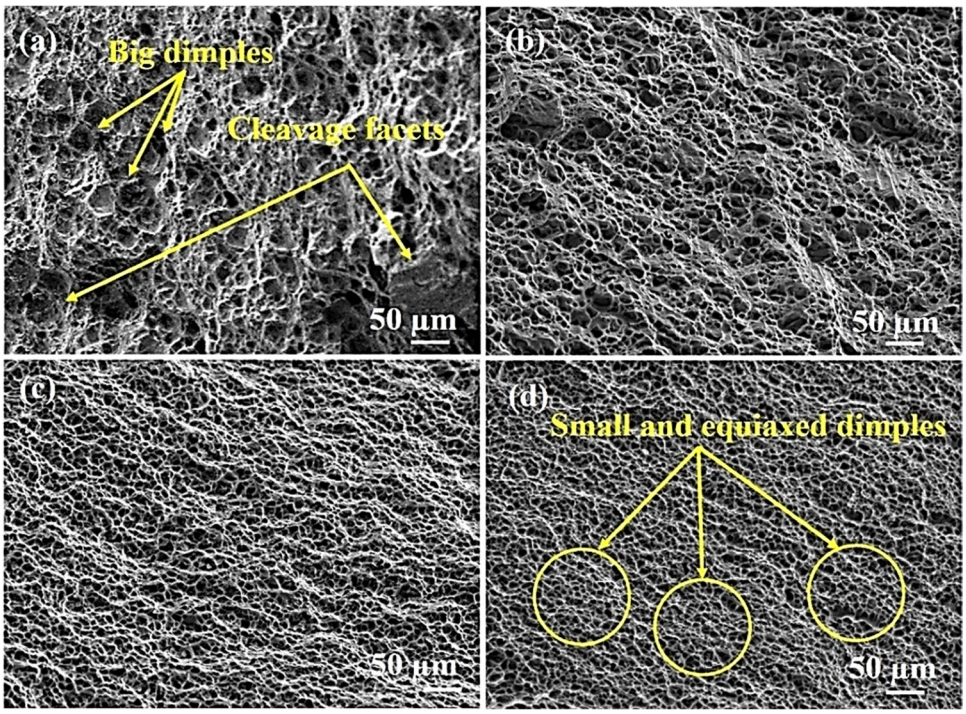

Fig. 11 Fracture images of MPFSP/($SiC + TiB_2$) of AA7050 hybrid composite, (**a**) 1st pass FSP, (**b**) 2nd pass FSP, (**c**) 3rd pass FSP, (**d**) 4th pass FSP

elongation, as you noted. This is because dislocations can act as obstacles to dislocation motion, which can make it more difficult for the material to deform plastically. As a result, the material may exhibit reduced ductility and elongation at fracture. It's worth noting that the presence of nanoparticles in the composite can also affect the deformation behavior and fracture mode of the material [71]. Nanoparticles can act as sources of stress concentration, which can promote the nucleation of voids or cracks and lead to a more brittle fracture mode. However, the fact that the fracture surface exhibited ductile features suggests that the nanoparticles were well-dispersed and did not significantly contribute to the materialization of cracks or voids. Cup-cone-like fractures were perceived in all the multipass samples.

Single pass FSP led to the refinement and redistribution of SiC and TiB_2 nanoparticles in the aluminum matrix, which prevented inter-dendritic crack propagation and resulted in increased ductility of the material. The fractured surface of the single-pass samples showed tiny dimples, indicating ductile fracture. 4 pass FSP samples showed tiny and equiaxed dimples with no cleavage facet, which revealed that the fracture was virtually ductile revealed in Fig. 11d. However, the material softening and coarse grain structure in the TMAZ and HAZ regions in the multiple-pass samples led to the rupture of the samples. The fractography of the samples was largely dependent on the dimples, nucleation and micro voids [31]. The increase in the FSP passes resulted in smaller dimples, which in turn led to an increase in the ductility and strength of the processed region after precipitation hardening. The TRS and input heat were perceived to have a relationship that influences the strength of the dissimilar joints. Excessive heat can reduce the tensile strength and encourage failure to happen in the TMAZ [72]. However, the dissemination of SiC and TiB_2 nanoparticles in the welded zone led to enhanced ductility and UTS of the joints due to the materialization of tiny dimples in the fractured surface. In the case of 4P FSP ($TiB_2 + SiC$)/AA7050 joints, the cluster particles were refined and redistributed, which removed the dendrite structure. The interdendritic crack propagation was prevented, and the flaws were distributed through the parent metals. This led to an enormous region of ductile and fine dimples in the fractured surface.

4 Conclusions

In this work, MPFSP ($TiB_2 + SiC$)/AA7050 surface composites were fabricated by MPFSP and two different nanoparticles, to examine the mechanical properties and microstructure of the processed region. The following conclusions from the above work have been drawn:

- The UTS of the MPFSP/($SiC + TiB_2$)/ AA7050 increased from 424 ± 5 to 561 ± 7 MPa as the number of FSP passes increased, which can be attributed to the fine grain structure and high fraction of high-angle grain boundaries obtained by MPFSP. Grain refinement can enhance the tensile properties of materials, including the UTS and % strain. A maximum tensile strength (561 ± 7 MPa) was perceived in 4P FSP (25% TiB_2,

75% SiC)/AA7050 due to the dissolution of coarse TiB_2, SiC and Mg_2Si, and grain refinement.

- The MPFSP (TiB_2 + SiC)/AA7050 perceived refined grains structure to have a higher microhardness value per the Hall–Petch relationship. The microhardness value was higher if the indenter was positioned neighboring the Mg_2Si rather than the α-Al. The maximum hardness value of 4pass FSP (25% TiB_2, 75% SiC)/AA7050 at the SZ was 179 HV, while the minimum microhardness value (161 HV) was perceived for 4P FSP (100% TiB_2)/AA7050. With the steady fall in the microhardness in the HAZ, the partially dissolved and strengthening phase coarsen in the HAZ, and some precipitates dissolve in the TMAZ region.
- The maximum joint efficiency of 132.30% was observed in 4P FSP (25% TiB_2, 75% SiC)/AA7050, while minimum joint efficiency of 111.39% was perceived in the 4P FSP (100% TiB_2)/AA7050. The MPFSP (TiB_2 + SiC)/AA7050 perceived refined grains structure to have a higher microhardness value per the Hall–Petch relationship. The maximum hardness value of 4pass FSP (25% TiB_2, 75% SiC)/AA7050 at the SZ was 179 HV, while the minimum microhardness value (161 HV) was perceived for 4P FSP (100% TiB_2)/AA7050.
- The homogenous distribution of the 2^{nd} phase particles within the aluminum matrix also contributed to the improvement in the UTS. This is because the 2^{nd} phase particles can act as obstacles to dislocation motion, which can strengthen the material.
- The dislocation movement in the grains occurs through large plastic deformation due to precipitation and dislocation strengthening. The hybrid composites contain varying amounts of TiB_2 and SiC nanoparticles with homogenous dispersion of TiB_2 and SiC particles, refined recrystallized grains, and high-quality interfacial bonding through the matrix was observed in 4^{th} pass FSP.

Author's Contribution Bharat Singh Chittoriya: Writing and reviewing of article.
Arvind Jayant, and Rakesh Kumar: Drafting and reviewing.

Data Availability All the data and information mentioned in this article are related to this research.

Declarations

Informed Consent Not applicable.

Consent for Publication No objection.

Consent to Participate No objection.

Conflict of Interest No.

Competing Interests No competing interests.

References

1. Varol T, Canakci A, Ozsahin S (2015) Modeling of the prediction of densification behavior of powder metallurgy Al-Cu-Mg/B4C composites using artificial neural networks. Acta Metall Sin 28:182–195
2. Hashmi AW, Mehdi H, Mishra RS, Mohapatra P, Kant N, Kumar R (2022) Mechanical Properties and Microstructure Evolution of AA6082/Sic Nanocomposite Processed by Multi-Pass FSP. Trans Indian Inst Met 75(8):2077–2090. https://doi.org/10.1007/s12666-022-02582-w
3. Suryanarayana C (2013) NasserAl-Aqeeli, Mechanically alloyed nanocomposites. Prog Mater Sci 58(4):383–502
4. Liao H et al (2021) Hybrid reinforced aluminum matrix composites fabricated by selective laser melting. Intermetallic 131:107080
5. Rani P, Mishra RS, Mehdi H (2022) Effect of Nano-sized Al2O3 particles on microstructure and mechanical properties of aluminum matrix composite fabricated by multipass FSW. Part C: J Mech Eng Sci (SAGE) https://doi.org/10.1177/09544062221110822.
6. Mehdi H, Mishra RS (2022) Consequence of reinforced SiC particles on microstructural and mechanical properties of AA6061 surface composites by multi-pass FSP. J Adhes Sci Technol 36(12):1279–1298. https://doi.org/10.1080/01694243.2021.1964846
7. Yi J et al (2021) In-situ chemical reaction mechanism and non-equilibrium microstructural evolution of (TiB2 + TiC)/AlSi10Mg composites prepared by SLM- CS processing. J Alloys Compd 857:157553
8. Suryanarayana C, Ivanov E (2013) 3 - Mechanochemical synthesis of nanocrystalline metal powders. In: Chang I, Zhao Y (eds) Advances in Powder Metallurgy. Woodhead Publishing, pp 42–68
9. Lieberthal M, Kaplan WD (2001) Processing and properties of Al2O3 nanocomposites reinforced with sub-micron Ni and NiAl2O4. Mater Sci Eng A 302:83–91
10. Sajjadi SA, Ezatpour HR, Beygi H (2011) Microstructure and mechanical properties of Al–Al2O3 micro and nano composites fabricated by stir casting. Mater Sci Eng A 528:8765–8771
11. AbuShanab WS, Abd Elaziz M, Ghandourah EI, Moustafa EB, Elsheikh AH (2021) A new fine-tuned random vector functional link model using Hunger games search optimizer for modeling friction stir welding process of polymeric materials. J Mater Res Technol 14:1482–1493
12. Abushanab WS, Moustafa EB, Melaibari AA, Kotov AD, Mosleh AO (2021) A novel comparative study based on the economic feasibility of the ceramic nanoparticles role's in improving the properties of the AA5250 nanocomposites. Coatings 11:977
13. Buha J, Lumley RN, Crosky AG (2008) Secondary ageing in an aluminium alloy 7050. Mater Sci Eng A 492(1):1–10
14. Jacumasso SC, Martins JDP, Carvalho ALMD (2016) Analysis of precipitate density of an aluminium alloy by TEM and AFM. Int Eng J 69(4):451–457
15. Mabuwa S, Msomi V, Mehdi H, Saxena KK (2022) Effect of material positioning on Si-rich TIG welded joints of AA6082 and AA8011 by friction stir processing. J Adhes Sci Technol 37(17):2484–2502. https://doi.org/10.1080/01694243.2022.2142366
16. Zhang X, Liu W, Liu SD, Deng YL (2009) 7050 aluminum alloy TTP curve. Chin J Nonferr Met 19(5):861–868

17. Komarasamy M, Alagarsamy K, Mishra RS, Ely L (2018) Characterization of 300 through thickness friction stir welded 7050–T7451 Al alloy. Mater Sci Eng A 716:55–62
18. Mishra RS, Ma ZY (2005) Friction stir welding and processing. Mater Sci Eng R 50(50):1–78
19 Mehdi H, Mishra RS (2022) Modification of Microstructure and Mechanical Properties of AA6082/ZrB2 Processed by Multipass Friction Stir Processing. J Mater Eng Perform 32(1):285–295. https://doi.org/10.1007/s11665-022-07080-0
20. Mehta KM, Badheka VJ (2019) Wear behavior of boron-carbide reinforced aluminum surface composites fabricated by Friction Stir Processing. Wear 426–427:975–980
21. Mehdi H, Mishra RS (2021) Effect of multi-pass friction stir processing and SiC nanoparticles on microstructure and mechanical properties of AA6082-T6. Adv Ind Manuf Eng 3:100062. https://doi.org/10.1016/j.aime.2021.100062
22. Tonelli L, Morri A, Toschi S, Shaaban M, Ammar HR, Ahmed MMZ, Ramadan RM, El-Mahallawi I, Ceschini L (2019) Effect of FSP parameters and tool geometry on microstructure, hardness, and wear properties of AA7075 with and without reinforcing B 2 C ceramic particles. Int J Adv Manuf Technol 102:3945–3961
23. Bisadi H, Abasi A (2011) Fabrication of Al7075/TiB2 Surface Composite via Friction Stir Processing. A J M Sci 2:67–70
24. Dwarakesh S, Puviyarasan M (2019) Experimental investigations on microstructure and mechanical properties of AA7075/SrCo3 composites fabricated using friction stir processing. Mater Today: Proceedings. https://doi.org/10.1016/j.matpr.2019.07.723
25. Bamane O, Patil S, Agarwal L, Kuppan P (2018) Fabrication and characterization of AA7075 metal matrix composite reinforced with MWCNT. Mater Today: Proceedings 5:8001–8007
26. Ahmadifarda S, Momenib A, Bahmanzadehb S, Kazemi S (2018) Microstructure, tribological and mechanical properties of Al7075 / Ti 3 AlC MAX-phase surface composite produced by friction stir processing. Vacuum 155:134–141
27. Kumar S, Kumar A, Vanitha C (2019) Corrosion behaviour of Al 7075 /TiC composites processed through friction stir processing. Mater Today: Proceedings 15:21–29
28. Patle H, Mahendiran P, Sunil BR, Dumpala R (2019) Hardness and sliding wear characteristics of AA7075-T6 surface composites reinforced with B 4 4 SiC C and MoS particles. Mater Res Express 6:086589. https://doi.org/10.1088/2053-1591/ab1ff4
29. Sharma A, Narsimhachary D, Sharma VM, Sahoo B, Paul J (2019) Surface modification of Al6061-SiC surface composite through impregnation of graphene, graphite & carbon nanotubes via FSP: A tribological study. Surf Coat Technol 368:175–191
30. Ande R, Gulati P, Shukla DK, Dhingra H (2019) microstructural and wear characteristics of friction stir processed Al7075/SiC reinforced aluminium composite. Mater Today: Proceedings 18:4092–4101
31. Gangil N, Maheshwari S, Siddiquee AN (2018) Novel Use of Distribution Facilitators and Time-Temperature Range for Strengthening in Surface Composites on AA7050-T7451. Metallogr Microstruct Anal 7:561–577. https://doi.org/10.1007/s13632-018-0474-x
32. Ma Y, Chen Z, Wang M, Chen D, Ma N, Wanga H (2015) High cycle fatigue behavior of the in-situ TiB2/7050 composite. Mater Sci Eng: A 640:350–356
33. Sharma DK, Patel V, Badheka V, Mehta K, Upadhyay G (2019) Fabrication of Hybrid Surface Composites AA6061/(B4C+MoS2) via Friction Stir Processing. ASME J Tribol 141(5):052201
34. Sharma DK, Patel V, Badheka V, Mehta K, Upadhyay G (2020) Different reinforcement strategies of hybrid surface composite AA6061/(B4C+ MoS2) produced by friction stir processing. Mater Sci Eng Technol 51(11):1493–1506
35. Sharma DK, Badheka V, Patel V, Upadhyay G (2021) Recent Developments in Hybrid Surface Metal Matrix Composites Produced by Friction Stir Processing: A Review. ASME J Tribol 143(5):050801
36. Akbari M, Khalkhali A, Keshavarz SME, Sarikhani E (2015) Investigation of the effect of friction stir processing parameters on temperature and forces of Al–Si aluminum alloys. Proc IMechE Part L: J Mater Des Appl 232(3):213–229
37. Akbari M, Asadi P (2021) Effects of different cooling conditions on friction stir processing of A356 alloy: Numerical modeling and experiment. Proc Inst Mech Eng C J Mech Eng Sci 236(8):4133–4146
38 Akbari M, Asadi P, Asiabaraki HR (2022) Investigation of Wear and Microstructural Properties of A356/ TiC Composites Fabricated by FSP. Surf Rev Lett 29(10):2250130
39. Akbari M, Asadi P, Aliha MRM, Berto F (2023) Modeling and optimization of process parameters of the piston alloy-based composite produced by FSP using response surface methodology. Surf Rev Lett 30(6):2350041
40. Akbari M, Aliha MRM, Berto F (2023) Investigating the role of different components of friction stir welding tools on the generated heat and strain. Forces in Mechanics 10:100166
41. Hashmi AW, Mehdi H, Mabuwa S et al (2022) Influence of FSP Parameters on Wear and Microstructural Characterization of Dissimilar TIG Welded Joints with Si-rich Filler Metal. SILICON 14:11131–11145. https://doi.org/10.1007/s12633-022-01848-8
42. Salah AN, Mabuwa S, Mehdi H et al (2022) Effect of Multipass FSP on Si-rich TIG Welded Joint of Dissimilar Aluminum Alloys AA8011-H14 and AA5083-H321: EBSD and Microstructural Evolutions. SILICON 14:9925–9941. https://doi.org/10.1007/s12633-022-01717-4
43. Adel Mahmood Hassan (2012) Tarek Qasim & Ahmed Ghaithan, Effect of Pin Profile on Friction Stir Welded Aluminum Matrix Composites. Mater Manuf Processes 27(12):1397–1401. https://doi.org/10.1080/10426914.2012.663238
44. Ali LF, Kuppuswamy N, Soundararajan R, Ramkumar KR, Sivasankaran S (2021) Microstructural evolutions and mechanical properties enhancement of AA 6063 alloy reinforced with Tungsten (W) nanoparticles processed by friction stir processing. Mater Charact 172:110903. https://doi.org/10.1016/j.matchar.2021.110903
45. Lombard H, Hattingh DG, Steuwer A et al (2008) Optimising FSW process parameters to minimise defects and maximise fatigue life in 5083–H321 aluminium alloy. Eng Fract Mech 75(3–4):341–354
46. Rahmatian B, Mirsalehi SE, Dehghani K (2019) Metallurgical and mechanical characterization of double-sided friction stir welded thick AA5083 aluminum alloy joints. Trans Indian Inst Met 72:2739–2751
47. Kim YG, Fujii H, Tsumura T et al (2006) Three defect types in friction stir welding of aluminum die casting alloy. Mater Sci Eng A 415(1–2):250–254
48. Guo Y et al (2018) An investigation on plasma-MIG hybrid welding of 5083 aluminum alloy. Int J Adv Manuf Technol 98(5–8):14331440

49. Wang J, Zhou D, Xie L, Li X, Lu Y, Bai Z, Zhou J (2021) Efect of multi-pass friction stir processing on microstructures and mechanical behaviors of as-cast 2A14 aluminum alloy. J Mater Eng Perform 30:3033–3043
50. Chen Y, Ding H, Cai Z, Zhao J, Li J (2016) Efect of initial base metal temper on microstructure and mechanical properties of friction stir processed Al-7B04 alloy Mater. Sci Eng A 650:396–403
51. Wang J, Yang K, Zhou D, Xie L, Lu Y, Li X (2021) Investigation on the microstructures and mechanical properties of friction stir processed 2A14 aluminum alloy fabricated by diferent initial precipitation states, The Int. J Adv Manuf Technol 116:3549–3560
52. He XC, Gu FS, Ball A (2014) A review of numerical analysis of friction stir welding. Prog Mater Sci 65:1–66
53. Jain S, Mishra RS (2021) Effect of Al2O3 nanoparticles on microstructure and mechanical properties of friction stir-welded dissimilar aluminum alloys AA7075-T6 and AA6061-T6. Proc Inst Mech Eng Part E: J Process Mech Eng 236(4):1511–1521
54. Jamalian HM, Ramezani H, Ghobadi H, Ansari M, Yari S, Givi MKB (2016) Processing–structure–property correlation in Nano-SiC-reinforced friction stir welded aluminum joints. J Manuf Process 21:180–189
55. Asadi P, Faraji G, Besharati Givi MK (2010) Producing of AZ91/SiC composite by Friction stir processing (FSP). Int J Adv Manuf Technol 51:247–260
56. Mehdi H, Mishra RS (2020) Influence of Friction Stir Processing on Weld Temperature Distribution and Mechanical Properties of TIG-Welded Joint of AA6061 and AA7075. Trans Indian Inst Met 73:1773–1788. https://doi.org/10.1007/s12666-020-01994-w
57. Akbari MK et al (2017) Al-TiB2 micro/nanocomposites: particle capture investigations, strengthening mechanisms and mathematical modelling of mechanical properties. Mater Sci Eng: A 682:98–106
58. Rahmani K, Majzoobi G, Atrian A (2018) A novel approach for dynamic compaction of Mg–SiC nanocomposite powder using a modified Split Hopkinson Pressure Bar. Powder Metall 61:164–177
59. Srivastava M, Rathee S, Siddiquee AN (2019) Investigation on the effects of silicon carbide and cooling medium during multi-pass FSP of Al-Mg/SiC surface composites. Silicon india 11:2149–2157
60. Liu Y et al (2012) Microstructure and mechanical properties of aluminum 5083weldments by gas tungsten arc and gas metal arc welding. Mater Sci Eng A 549:7–13
61. Barmouz M, Givi MKB (2011) Fabrication of in situ Cu/SiC composites using multi-pass friction stir processing: Evaluation of microstructural, porosity, mechanical and electrical behavior. Compos A Appl Sci Manuf 42(10):1445–1453
62. McLean AA, Powell GLF, Brown IH, Linton VM (2003) Friction stir welding of magnesium alloy AZ31B to aluminium alloy 5083. Sci Technol Weld Joining 8(6):462–464
63. Ralls AM, Kasar AK, Menezes PL (2021) Friction Stir Processing on the Tribological, Corrosion, and Erosion Properties of Steel: A Review. Manuf Mater Process 5(3):97. https://doi.org/10.3390/jmmp5030097
64. Chang CI, Lee CJ, Huang JC (2004) Relationship between grain size and Zener-Holloman parameter during friction stir processing in AZ31 Mg alloys. Scripta Mater 51:509–514
65. Oladijo OP, Venter AM, Cornish LA, Sacks N (2012) X-ray diffraction measurement of residual stress in WC-Co thermally sprayed coatings onto metal substrates. Surf Coat Techno 206:4725–4729
66. Paidar M (2019) Olatunji Oladimeji Ojo, Hamid Reza Ezatpour, Influence of multi-pass FSP on the microstructure, mechanical properties and tribological characterization of Al/B C composite fabricated by accumulative roll bonding (ARB). Surf Coat Technol 361:159–169
67. Tariq M, Khan I, Hussain G, Farooq U (2019) Microstructure and micro-hardness analysis of friction stir welded bi-layered laminated aluminum sheets. Int J Light Mater Manuf 2(2):123–130
68 Patel VV, Badheka V, Kumar A (2017) Effect of polygonal pin profiles on friction stir processed superplasticity of AA7075 alloy. J Mater Process Technol 240:68–76
69. Qin H, Zhang H, Wu H (2015) The evolution of precipitation and microstructure in friction stir welded 2195–T8 Al–Li alloy. Mater Sci Eng A 626:322–329
70. Butola R (2020) Murtaza, Qasim, Singari, Ranganath M, Formation of Self-Assembled Monolayer and Characterization of AA7075-T6/B4C Nano-ceramic surface composite using Friction Stir Processing. Surf Topogr Metrol Prop 8(2):025030
71. Deore HA, Bhardwaj A, Rao AG, Mishra J, Hiwarkar VD (2020) Consequence of reinforced SiC particles and post process artificial ageing on microstructure and mechanical properties of friction stir processed AA7075. Def Technol 16:1039–1050
72. Karakizis PN, Pantelis DI, Fourlaris G et al (2018) Effect of SiC and TiC nanoparticle reinforcement on the microstructure, microhardness, and tensile performance of AA6082-T6 friction stir welds. Int J Adv Manuf Technol 95:3823–3837. https://doi.org/10.1007/s00170-017-1446-z